

# A laser-induced breakdown spectroscopy method to assess the stochasticity of plasma-flame transition in sprays

Pedro M de Oliveira<sup>1,‡,\*</sup>, Michael Philip Sitte<sup>2</sup>, Maria Kotzagianni<sup>1</sup>, Patton M Allison<sup>3</sup>  
and Epaminondas Mastorakos<sup>1</sup>

<sup>1</sup> Hopkinson Laboratory, Department of Engineering, University of Cambridge, Cambridge, United Kingdom

<sup>2</sup> Siemens Mobility GmbH, Vienna, Austria

<sup>3</sup> Department of Mechanical Engineering, Michigan State University, East Lansing, MI, United States of America

E-mail: [pm580@cam.ac.uk](mailto:pm580@cam.ac.uk)

Received 20 January 2022, revised 26 April 2022

Accepted for publication 27 May 2022

Published 8 June 2022



CrossMark

## Abstract

An experimental approach is presented to evaluate the impact of plasma composition arising from pulse-to-pulse energy and mixture fluctuations on the non-resonant laser-induced ignition of sprays. This allows for spark events to be conditioned on the successful or failed establishment of a flame kernel, a phase dominated by plasma decomposition and recombination reactions and the on-set of combustion reactions, that is, independent of the subsequent flame growth phase controlled by propagation phenomena only, such as fuel availability and turbulent strain. For that, laser-induced breakdown spectroscopy of the spark-generated plasma is carried out, followed by OH\* high-speed imaging of the kernel. Exploratory experiments in spatially uniform and polydisperse kerosene droplet distributions in a jet suggest that the hydrogen concentration in the plasma deriving from the fuel dissociated by the spark is closely related to the generated OH\* radicals levels and, in turn, with the success of establishing a flame kernel. This suggests that the ignition process is heavily controlled by mixture fluctuations at the spark, inherent of spray flows. The instantaneous mixture at the spark is estimated with a stochastic model, with the probability density function of the equivalence ratio exhibiting values higher than twice the mean value, while the highest probability occurs at lean conditions between the gaseous equivalence ratio and the overall equivalence ratio. The findings corroborate insights on the early-phase ignition obtained from direct numerical simulations, and the framework paves the way for the development of smart online engine-health tools to assess relight capability in future aeroengines.

‡ I am honoured and grateful to the editorial board of Measurement Science & Technology for my nomination as one of 2022's *Emerging Leaders* in measurement and metrology. I am glad to co-author this work with colleagues who were instrumental to my research on spray flames, as we present key concepts for the application of LIBS to unveiling the stochasticity of ignition processes in sprays.

\* Author to whom any correspondence should be addressed.



Original Content from this work may be used under the terms of the [Creative Commons Attribution 4.0 licence](https://creativecommons.org/licenses/by/4.0/). Any further distribution of this work must maintain attribution to the author(s) and the title of the work, journal citation and DOI.

Keywords: laser-induced breakdown spectroscopy, LIBS, ignition, plasma-flame transition, spray combustion, polydisperse sprays

(Some figures may appear in colour only in the online journal)

## Nomenclature

$A_f$	Projected flame area
$d$	Droplet diameter
$d_{10}$	Mean diameter
$d_{32}$	Sauter mean diameter
$d_s$	Spark diameter
$E_{\text{abs}}$	Absorbed laser energy
$E_{\text{in}}$	Incident laser energy
$E_{\text{trans}}$	Transmitted laser energy
$I$	Intensity
$m$	Mass
$\dot{m}$	Mass flow rate
$n$	Number density
$N$	Number of droplets
$p$	Binomial single trial success probability
$P$	Probability
$q$	Rosin–Rammler shape parameter
$Q$	Cummulative volume density function
$t$	Time
$T$	Temperature
$V_0$	Unit volume
$V_c$	Control volume
$X$	Rosin–Rammler scale parameter
$\lambda$	Wave length
$\mu$	Poisson rate parameter
$\rho$	Density
$\phi$	Equivalence ratio
$\phi_g$	Gaseous equivalence ratio
$\phi_l$	Liquid equivalence ratio
$\phi_o$	Overall equivalence ratio
$\bar{\cdot}$	Average
DNS	Direct numerical simulation
FAR	Fuel-to-air ratio
LIBS	Laser-induced breakdown spectroscopy
pdf	Probability density function
SMD	Sauter mean diameter

## 1. Introduction

The ignition of a flame in a two-phase flow is of great relevance to aeroengines and liquid-propellant rocket engines. Besides the characteristics of the spark, successful ignition of a combustor is dependent on the local (and instantaneous) flow and mixture conditions at the spark, impacting the creation of a flame kernel, as well as globally at the combustor, and affecting the subsequent growth of the flame and its stabilisation [1]. Laser-induced breakdown spectroscopy (LIBS) has been used as a point-wise technique to evaluate the time-averaged air-fuel equivalence ratio of gaseous mixtures [2–5] and sprays [6, 7]. A motivation for the use of LIBS to combustion problems is that, conveniently, laser-induced breakdown can also be used to enhance ignition [8]. It has the advantage of forming

a flame kernel within a region of the combustor most conducive to ignition, for example, near the spray cone and recirculation zones [9]. Thus, there are potentially great benefits in using LIBS for online mixture probing [10] and simultaneous ignition monitoring, for example, through the development of engine-health diagnostics that can monitor the capability of high-altitude relight of an aircraft—a process defining the engine’s operation envelope. For that, the relationship between the characteristics of the spark plasma and the subsequent conventional combustion behaviour of the spray must be understood. This work provides an experimental framework towards the development of such tools.

LIBS has been used to reveal aspects of the plasma-flame transition in gaseous mixtures, providing evidence that radical generation during the cooling of the plasma may be a key factor in the growth of a flame kernel. Beduneau *et al* [11] verified that, following the initial decay of  $\text{OH}^*$ ,  $\text{CH}^*$ ,  $\text{C}_2^*$ , and  $\text{CN}^*$  radical emissions, a rise of emissions of those radicals occurred only in *ignition* events—here, loosely defined as the appearance of a flame—while the impact of the initial size of the kernel did not seem to be as determining to the process [11].

In sprays, however, the initial size of the kernel was observed to be closely related to ignition success [12], attributed both to the availability of fuel at the moment and location of the spark and to the optical effects droplets have on the laser beam. The presence of droplets may enhance laser ignition by simply decreasing the threshold energy necessary for breakdown [13] and therefore increasing the probability of breakdown by the laser [12, 14]. Still, their effects on the resulting plasma composition and, in turn, on the establishment of a kernel are not well understood. Furthermore, experiments carried out by Gebel *et al* [15] have provided the first assessment of the plasma characteristics during spray ignition. By comparing the evolution of the LIBS spectra of fuel in air to those in a nitrogen atmosphere, they found that recombination processes in the decaying plasma giving rise to  $\text{C}_2^*$  and  $\text{CN}^*$  occurred in both atmospheres, while  $\text{CH}^*$  formation occurred only in air-fuel mixtures, thus suggesting that  $\text{CH}^*$  must be formed through combustion reactions of reactants in the radical pool rather than plasma recombination. Despite the interesting findings, successful ignition was always guaranteed in the air-fuel experiments by using high-energy sparks of 200 mJ. This approach limits the understanding of the process and its application to realistic spark conditions where ignition failure in a combustible mixture is prone to occur.

Correlating ignition to the local mixture conditions is not straightforward. First, ignition is a highly stochastic process, sensitive to the fluctuations found in a combustor, from turbulence to energy deposition fluctuations [1]. Ignition itself is a term that is often not well defined in the literature. When does the transition from the spark plasma into a flame occur,

and how can one differentiate and quantify the impact that fuel fluctuations have on two very distinct phases—the first depending on thermal runaway and the following on propagation phenomena? Second, mixture fluctuations are inherent to sprays, as most of the fuel is concentrated in the liquid droplets which occupy a small volume fraction and are often of similar size to the laser probing volume. Finally, LIBS has an inherent uncertainty for evaluating mixture composition because the breakdown plasma is formed through a stochastic process prone to fluctuations that control the absorption of laser energy by the flow. If the mixture brings its own fluctuations, either temporal (i.e. pulse-to-pulse) or spatial (i.e. inhomogeneities at the scale of the plasma volume), the interpretation of the LIBS signal involves uncertainties that must be understood for accurate utilisation of the technique for combustion processes.

This work puts forward an experimental approach combining LIBS and OH\* chemiluminescence imaging to characterise the plasma generated by the spark conditioned to the outcome of an ignition attempt, that is, failure or success of establishing a flame kernel and a self-sustained flame. For that, a brief revision of terms and definitions concerning the ignition is first provided, building upon the understanding of ignition phases as defined by Lefebvre [20] and Mastorakos [1, 16]. Experiments are performed in a canonical and well-characterised flow comprising of uniformly distributed droplets in a jet. The effects of the local instantaneous equivalence ratio at the laser spark on the emission intensities of atomic lines and molecular bands such as H $\alpha$ , CN\*, C $_2$ \*, O and N in the plasma are investigated by using polydisperse sprays with different Sauter mean diameters ( $SMD = d_{32}$ ). A stochastic approach is proposed to estimate the degree of equivalence ratio fluctuations expected at the spark location. Pulse-to-pulse laser energy measurements are carried out to reveal the impact of energy fluctuations on the process.

## 2. Methods

### 2.1. Definitions and phases of ignition

The definitions used by various authors concerning the early phases of ignition are not always clear or consistent, often giving rise to ambiguities. Here, a time scale concerning the relative duration of spark effects on the flame kernel is used as a reference to distinguish between the phases of kernel generation and flame growth, represented by the red line in figure 1. With that, relevant time scales and other ignition-related definitions from the literature are consolidated. The time scale concerning the *spark effects on the flame* is defined as the time when a net increase of chain-branching reactions over recombination reactions occurs [18], evaluated here as the time at which approximately constant OH\* emissions relative to the size of the kernel are observed. In numerical works, it could also be understood as the time at which the maximum temperature of the flame kernel reaches a stable value, being approximately the adiabatic flame temperature [17]. Further, in this work, a *spark event, or ignition attempt* is simply every laser pulse in which breakdown of the mixture is attempted. A *flame*

*kernel* is loosely defined as the region of the flow from the moment breakdown occurs and a plasma is formed, up to its transition into a self-sustained flame, being characterised by a length scale shorter than the flow's integral length scale and a time scale shorter than the bulk flow time scale [16]<sup>4</sup>. Further, the *formation of a kernel*, or its initiation, depends solely on breakdown of the mixture by the laser, generating a hot plasma—that is, completion of Phase Ia. Following this, the *establishment of a kernel* occurs if combustion reactions are successfully kick-started and are followed by a net increase of chain-branching reactions, hence representing the successful completion of Phase I. The transition from plasma to flame during Phase I is the focus of this work.

Next, if the flame kernel continues to grow, a *self-sustained flame* is obtained and marks the end of Phase II. The self-sustained flame has a length scale larger or of the order of the flow's integral length scale, while its time scale is longer or of the order of the bulk flow time scale [16]. Failure to ignite occurring after a short duration relative to the spark [16] is then referred to as the *short mode of ignition failure*. Here, this represents failure during Phase I, being evaluated based on the complete decay of OH\* emissions occurring earlier than the average duration of the spark effects on the flame. Similarly, failure to ignite that occurs long relative to the spark is referred to as the *long mode of ignition failure* [16], representing failure during Phase II. Finally, in the present experiments, *ignition* is defined simply as the establishment of a self-sustained flame at the end of Phase II—as no stabilisation mechanism of the flame is present in this experiment, Phase III is not possible. For experimental works aiming at investigating issues such as minimum ignition energy, it may be convenient to define the *probabilities of breakdown, kernel establishment, and flame and burner ignition*, based on the number of successful events in which completion of Phases Ia, Ib, II, and III, respectively, is achieved, relative to the total number of events.

### 2.2. Experimental setup

The jet spray burner used in the present work (figure 2(b)) has been previously discussed in detail [12, 22]. Thus, only its main features, relevant to the present work, are given. The burner consists of a diverging-converging tube (1) where Jet A-1 fuel [23] is atomised by an air-assist atomiser (2) in an air stream, exiting through a 20.8 mm diameter nozzle (detail A). This forms an open jet, characterised by uniform velocity, turbulence, and droplet size distribution profiles in the radial direction and within one jet diameter downstream. The droplet size distribution is controlled by adjusting the liquid and air flow rates into the atomiser. The overall equivalence ratio of the flow, that is, the ratio of global fuel and air mass flow rates

<sup>4</sup> The flow integral time scale  $T_{\text{turb}}$  can be obtained by integrating the normalised autocorrelation coefficient of the velocity measurement. In this work, measurements were previously carried out with laser doppler anemometry. The integral length scale is then estimated as  $L_{\text{turb}} = T_{\text{turb}} \times U_b$ , where the latter parameter is the flow bulk velocity. Here,  $T_{\text{turb}} = 1.2$  ms, which results in  $L_{\text{turb}} = 9.5$  mm, that is, approximately half of the jet diameter, as expected. More details on length and time scales of turbulent flows can be found in [21].

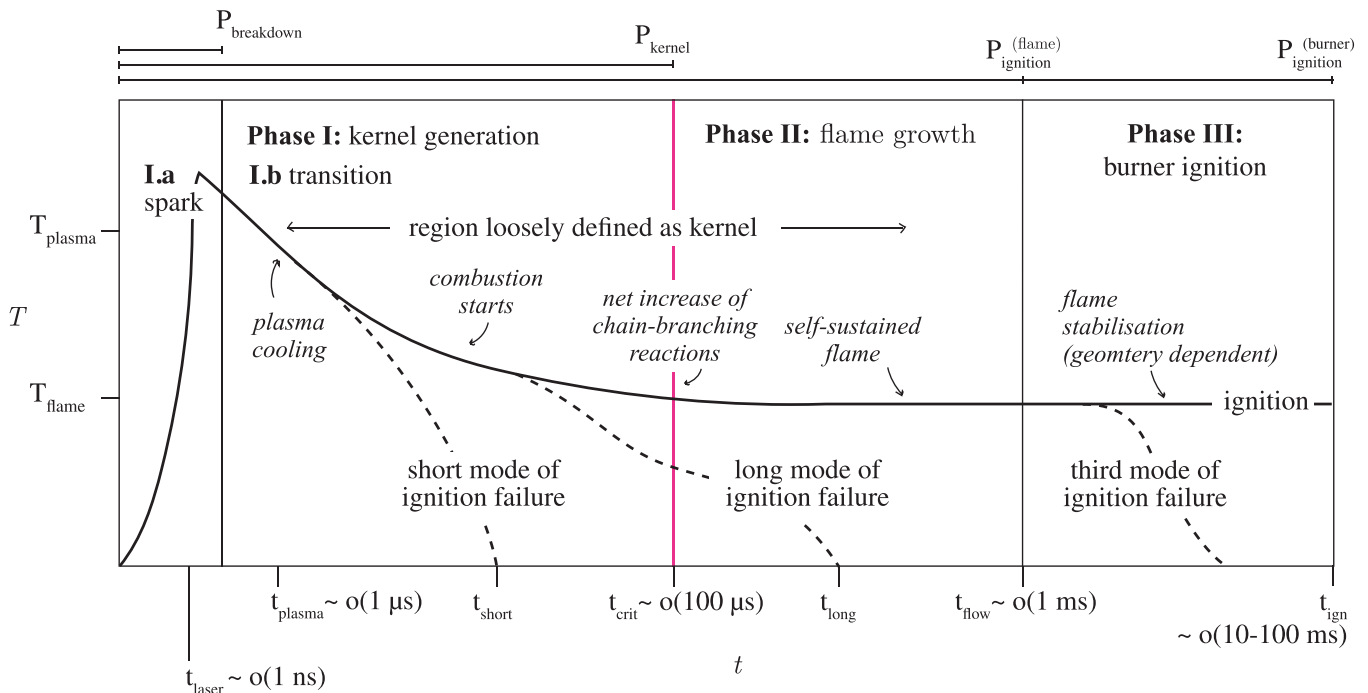


**Figure 1.** Ignition time scales and relevant definitions. The plot illustrates the maximum flame kernel in respect to the time after the spark. The figure consolidates findings from previous experiments and simulations [1, 8, 11, 12, 16–19] and shows a critical time scale (red line) used to distinguish between the kernel generation phase and flame growth phase.

supplied to the burner relative to the stoichiometric fuel-to-air ratio,  $\phi_o = (\dot{m}_{\text{fuel}}/\dot{m}_{\text{air}})/\text{FAR}_{\text{st}}$ , is set to 0.8 with the mass flow rate of fuel  $\dot{m}_{\text{fuel}} = 0.133 \text{ g s}^{-1}$  and air  $\dot{m}_{\text{air}} = 2.364 \text{ g s}^{-1}$ . The stoichiometric fuel-to-air ratio,  $\text{FAR}_{\text{st}}$ , is the mass ratio of  $(m_{\text{fuel}}/m_{\text{air}})$  at stoichiometric conditions, being 0.07032 for kerosene. Within the region of interest the gas-phase equivalence ratio, based on the mass of fuel vapour and air,  $\phi_g = (m_{\text{vap}}/m_{\text{air}})/\text{FAR}_{\text{st}}$ , is evaluated to be 0.3 [22], as the spray is partially prevaporised by setting the main carrier air flow temperature to  $100^\circ\text{C}$ . The two-phase jet formed immediately downstream of the burner nozzle is characterised by a poly-disperse size distribution, evaluated in a previous work by the authors [22] through particle Doppler anemometry measurements. From measurements of the SMD with phase Doppler anemometry, three distinct conditions of the spray immediately downstream of the jet nozzle are chosen for experiments: 16, 23, and  $27 \mu\text{m}$ . Modified Rosin–Rammler distributions were obtained for the three spray conditions [22], with the shape parameter  $q$  being 5.04, 6.12, and 7.23, and the scale parameter  $X$  being 27.9, 38.0, and 44.7, from fine to coarse spray, respectively.

The jet was ignited with a 532 nm 5 ns beam generated with an Nd:YAG laser (Continuum Surelite II). Second-harmonic generation was chosen for convenience, as non-resonant laser-induced breakdown is independent of laser wavelength [8] and enough energy, for the purposes of this work, was available at 532 nm. The ignition optical path consisted of a telescope (3,  $-30 \text{ mm}$  plano-concave lens and  $75 \text{ mm}$  plano-convex lens) to expand the beam prior to focusing with a  $30 \text{ mm}$  plano-convex lens near the edge of the flow. The laser was fired at 2 Hz so that events were completely independent from

each other. A photodiode at the laser output was used to sync the laser pulse, an intensified camera for  $\text{OH}^*$  chemiluminescence, and the spectrometer system to evaluate the plasma emissions after breakdown of the mixture. The  $\text{OH}^*$  chemiluminescence was imaged after a  $100 \mu\text{s}$  delay from the spark at 12 kHz with an exposure time of  $80 \mu\text{s}$ . An additional high-speed camera with the same frequency and exposure settings was used with schlieren optics for visualisation of the flow [12]—used here for the sole purpose of illustrating the problem investigated. The incident energy was kept at 23 mJ and 47 mJ by adjusting the Q-switch delay of the laser throughout the experiments. Pyroelectric energy sensors are used to evaluate the incident (4, partially reflected by a beam splitter) and the transmitted laser energies (5),  $E_{\text{in}}$  and  $E_{\text{trans}}$ , for each spark. An approximate 5% pulse-to-pulse variation of the incident energy was evaluated experimentally, that is,  $\pm 1.2$  and  $\pm 2.5 \text{ mJ}$  for the low and high energy cases (confidence interval of 95%). The absorbed energy for each condition, evaluated simply as  $E_{\text{in}} - E_{\text{trans}}$ , is lower than the incident value; measurements are given in the results section. The systematic uncertainty [24] of the air mass flow rate was approximately 2% and 1% for the carrier and atomising air, respectively, and 0.2% for the liquid mass flow rate, thus resulting in a derived experimental uncertainty [25] for  $\phi$  of approximately  $\pm 0.3\%$  (confidence interval of 95%). A systematic uncertainty of 3% was associated to the incident and transmitted laser energy measurements, and a combined uncertainty for the absorbed energy was evaluated using the Taylor series method for propagation of uncertainties described in [25], being typically around 0.8 and 1.6 mJ for the low and high incident energy, respectively.

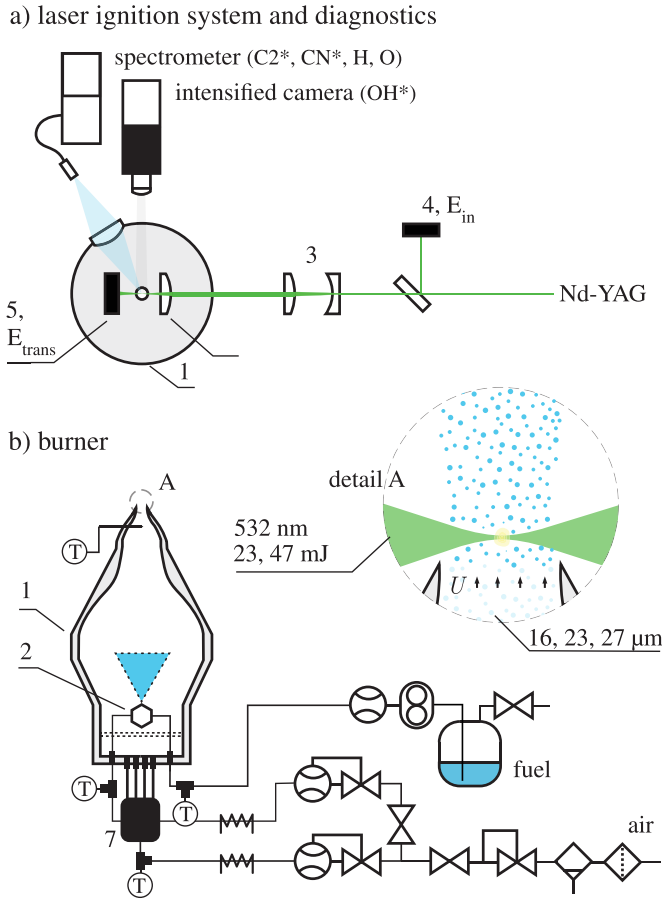


**Figure 2.** Schematics of the (a) laser ignition and diagnostics systems and (b) the jet spray burner. The apparatus produces a uniform droplet distribution in a jet, characterised by a polydisperse spray, top-hat velocity profile, and well-defined gaseous phase. The growth of the flame following a laser spark is observed immediately downstream the nozzle. Plasma emissions are collected for each spark attempt, and the OH\* is imaged with an intensified high-speed camera. Energy measurements are carried out for each spark. Modified from [12].

Given breakdown of the mixture occurs for a specific laser spark, the flame kernel may grow or quench while it is convected by the bulk flow at approximately  $8 \text{ m s}^{-1}$ . The growth or quenching of a given flame kernel was determined from its projected flame area,  $A_f$ , obtained from post-processing of the OH\* image sequence. From all ignition events, a critical timescale concerning the effects of the spark on the flame was obtained based on the decay of the average value of OH\*/ $A_f$  to an approximately asymptotic value [12]. Based on that, events were categorised as short-mode failure, long-mode failure, in addition to ignition, as shown in figure 1. In all spark events, the plasma emission light for each individual spark attempt was collected and classified based on the ignition attempt outcome. The emission light was collected using a large 100 mm convex lens and an optical fibre connected to an echelle spectrometer (Andor Mechelle 5000,  $50 \times 50 \mu\text{m}$  entrance slit, 52.13 lines  $\text{mm}^{-1}$  grating blazed at  $32.35^\circ$ , reciprocal dispersion  $1\text{--}4.5 \text{ nm mm}^{-1}$ ) and an ICCD camera (Andor iStar,  $1024 \times 1024$  pixels,  $13 \mu\text{m}$  pixels) to record the signal (0.1 nm

FWHM spectral resolution). A delay of  $1 \mu\text{s}$  was set in relation to the laser pulse, and the plasma emission was collected with an exposure time of  $50 \mu\text{s}$ . The spectrometer was calibrated with a Hg–Ar light prior to the experiments.

### 2.3. Mixture fluctuation estimation

Two-phase reacting flows have significant mixture inhomogeneities. Most importantly, a significant fraction of fuel is concentrated in the liquid droplets, which only occupy a very small volume fraction due to much higher density than the gas phase. As a result of the random motion of droplets in a turbulent flow and the random break-up of droplets in the atomisation process, mean spray properties converge in a statistical sense when the sampling volume is large and the number of droplets in a small volume exhibits stochastic fluctuations.

In order to estimate the fluctuations of local equivalence ratio expected in a small (spark) volume for a monodisperse spray, a stochastic approach is employed, under the single assumption of uniform spatial distribution of droplets [26]. Assuming the unit volume  $V_0$  with precisely  $N_0$  droplets randomly distributed, the number of droplets  $N_c$  that is found in a small control volume  $c$ ,  $V_c < V_0$ , follows a binomial distribution

$$P(N_c) = \binom{N_0}{N_c} p^{N_c} (1-p)^{N_0-N_c} \quad (1)$$

where the parameter  $p = V_c/V_0$  represents the success probability for each trial.

The binomial distribution can be approximated by a Poisson distribution if  $N_0$  is large and  $p = V_c/V_0$  is small. Both assumptions usually hold for sprays of technical interest and small sparks. Additionally, it is convenient to describe the number of droplets by a mean number density, defined as the mean number of droplets in a unit volume,  $n = \bar{N}_0/V_0$ , which is not limited to integer values. Following the Poisson distribution, the probability of finding exactly  $N_c$  droplets in the volume  $V_c$  is

$$P(N_c) = \frac{e^{-\mu} \mu^{N_c}}{N_c!} \quad (2)$$

where  $\mu$  is the expected value of the number of droplets in the spark volume,  $\mu = nV_c$ . Analogue to the gaseous equivalence ratio a liquid equivalence ratio, based on the mass ratio of liquid fuel and air,  $\phi_l = (m_l/m_{\text{air}})/\text{FAR}_{\text{st}}$ , is introduced. Then the liquid equivalence ratio in  $V_c$  is

$$\phi_l = \frac{N_c}{nV_c} \bar{\phi}_l \quad (3)$$

where  $N_c$  is the stochastic variable given by equation (2) and  $\bar{\phi}_l$  is the expected value of  $\phi_l$ . Here, the case of a spatially uniform distribution was used for graphical purposes. Formulations based on time-average for statistically stationary flow or an ensemble average for a transient flow are equivalent.

Most sprays of practical interest have a polydisperse character where droplets span a range of sizes. These size characteristics of the spray can be described statistically by

means of a size distribution. Under statistically stationary conditions, this distribution is obtained experimentally with a long sampling time, corresponding to the time-averaged flow field. In general, this distribution will depend on the location in the flow. A commonly used statistical model is the Rosin–Rammler distribution, which is used to fit the droplet volume distribution. Then the cumulative volume density function is

$$Q(d) = 1 - \exp \left[ - \left( \frac{d}{X} \right)^q \right] \quad (4)$$

where  $X > 0$ ,  $q > 0$  are the parameters of the distribution that can be related to the statistical moments of the spray, e.g.  $d_{10}$  and  $d_{32}$  [27]. Alternatively, sometimes a *modified* Rosin–Rammler function, where  $(d/X)$  is replaced by  $(\ln d / \ln X)$ , is used to better fit the small-size range [28].

The droplet number distribution (i.e. pdf of droplet diameter) can be obtained from the cumulative volume density function as follows:

$$\text{pdf}(d) = \frac{1}{\int_0^\infty \frac{6}{\pi d^3} \frac{dQ}{dd} dd} \frac{6}{\pi d^3} \frac{dQ}{dd}(d) \quad (5)$$

where  $dQ/dd$  is the volume distribution function. The pdf is normalised dividing by its integral.

For a polydisperse spray, the reasoning from equation (2) can be applied to droplet classes containing all droplets of similar size, under the assumptions that (a) droplets of each size class are uniformly distributed in space and (b) that droplets of different size classes are independent of each other, i.e. *independent and identically distributed*. Then the liquid equivalence ratio in  $V_c$  is [26]

$$\phi_1 = \sum_{i=1}^{\infty} \Delta Q_i \frac{N_{i,c}}{n_i V_c} \bar{\phi}_1 \quad (6)$$

where  $\Delta Q_i$  is the the fraction of liquid volume contained in droplets of size class  $i$  (from equation (4)),  $n_i$  is the droplet number density of size class  $i$ ,  $N_{i,c}$  is the stochastic number of droplets in  $V_c$ , which follows equation (2) with  $\mu_i = n_i V_c$ .

If the spray is partially prevaporised, some fuel may be present in gaseous form, which is characterised by the gaseous equivalence ratio,  $\phi_g$ . The total equivalence ratio in  $V_c$  is

$$\phi = \phi_g + \phi_1. \quad (7)$$

### 3. Results and discussion

#### 3.1. Fluctuations

**3.1.1. Mixture conditions.** An important aspect of spray ignition—in particular, laser ignition with small spark volumes—is the presence (or absence) of droplets in the spark volume. This aspect can be understood using the stochastic approach presented in section 2.3 to describe the fluctuations of the local equivalence ratio in a spark volume. The model is applied here to the experimental cases described in section 2.2: kerosene fuel and air supply mass flow rates  $\dot{m}_{\text{fuel}} = 0.133 \text{ g s}^{-1}$ ,  $\dot{m}_{\text{air}} = 2.364 \text{ g s}^{-1}$ , so that  $\phi_0 = 0.8$

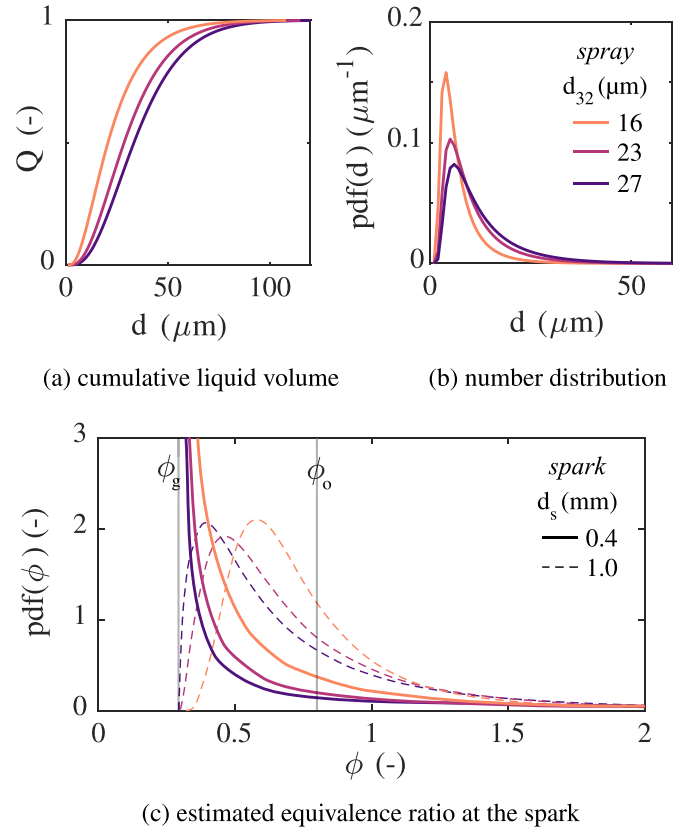


**Figure 3.** (a) Cumulative liquid volume distribution, (b) number distribution, and (c) pdf of resulting equivalence ratio at the spark location. Overall equivalence ratio  $\phi_0$  and gaseous equivalence ratio  $\phi_g$  are indicated by vertical lines.

( $\text{FAR}_{\text{st}} \approx 0.07032$ ). At the region of interest  $\phi_g = 0.3$  and, as a result, the mean liquid equivalence ratio is estimated to be  $\bar{\phi}_1 = \phi_0 - \phi_g = 0.5$ .

For three measured flow conditions with SMD  $d_{32} = 16$ , 23 and 27  $\mu\text{m}$ , *modified* Rosin–Rammler volume distributions are presumed with  $X$  and  $q$  parameters given in section 2.2. For those flow conditions, the cumulative volume distributions are shown in figure 3(a). The corresponding number distributions (equation (5)) are shown in figure 3(b) for reference. They illustrate the characteristic high number of small droplets in a polydisperse spray, which account for only a fraction of the total fuel volume. Two spark conditions were studied with spark diameters  $d_s = 0.4$  and 1 mm corresponding to the two incident energies of 23 and 47 mJ, respectively. The plasma diameter was estimated by imaging the bremsstrahlung radiation of the plasma in air [12].

The model was evaluated using a Monte Carlo approach. The droplet size range,  $1 \leq d \leq 200 \mu\text{m}$ , was divided into approximately one thousand size classes. For each bin,  $i$ , the mean number density  $n_i$  is estimated as follows. The bulk volume flow rate at the region of interest is approximately computed from the supply air volume flow rate to be  $\dot{m}_{\text{air}}/\rho_{\text{air}}$ . It is very little affected by the presence of the (dilute) spray, but the effect of evaporative cooling was taken into account when evaluating the gas density,  $\rho_{\text{air}}$ , at  $T \approx 80^\circ\text{C}$ . The liquid fuel mass in the region of interest was estimated taking into

account the prevaporisation, so that the remaining mean liquid fuel mass flow rate at the spark location is  $(\bar{\phi}_l/\phi_o)\dot{m}_{\text{fuel}}$ . It follows that the number density for size class  $i$  can be estimated as

$$n_i \approx \frac{\Delta Q_i (\bar{\phi}_l/\phi_o) \dot{m}_{\text{fuel}}/(\rho_l d_i^3 \pi/6)}{\dot{m}_{\text{air}}/\rho_{\text{air}}} \quad (8)$$

where  $\Delta Q_i$  represents the fraction of liquid volume contained in droplet size class  $i$ . The spark size was defined by the spark diameter  $d_s$ . The relevant control volume representative of the spark was  $V_c = d_s^3 \pi/6$ .

In the Monte Carlo simulations, a sample of one million random numbers  $N_{c,i}$  is generated for each size class  $i$ , following a Poisson distribution (equation (2)) with the parameter  $\mu_i = n_i V_c$ . Using equation (6) a sample of one million possible outcomes for the liquid equivalence ratio in the spark volume,  $\phi_l$ , is computed. The equivalence ratio at the spark location is given according to equation (7). Here the gaseous equivalence ratio,  $\phi_g$ , is assumed constant, i.e. without stochastic fluctuations due to complete prevaporisation and premixing upstream of the section of interest. Finally, the degree of mixture fluctuations expected at the spark location, that is, the pdfs of the total equivalence ratio at the spark location for the three spray conditions and two spark diameters are presented in figure 3(c).

Note that the expected value from all pdfs of  $\phi$  is equal to the overall equivalence ratio  $\phi_o$  in the present case with stationary uniform flow conditions, so that  $\bar{\phi} = \phi_g + \bar{\phi}_l = \phi_o$ . Since  $\phi_g$  is approximately constant, all fluctuations of  $\phi$  are associated with  $\phi_l$ . Fluctuations of the equivalence ratio increase with droplet size and decrease with spark size. For the larger spark, the statistic converges and the pdf narrows around  $\phi_o$ . In contrast, for larger droplets the pdf widens with a higher probability for lean or rich mixture. Additionally the influence of two further parameters should be noted: (a) fluctuations decrease with the degree of prevaporisation since the gap between  $\phi_g$ , also representative of the minimum equivalence ratio, and the expected value  $\phi_o$  narrows; (b) fluctuations are higher for a polydisperse spray—such as considered here—compared to a monodisperse spray, since relatively few large droplets may contain a large fraction of the total amount of fuel.

**3.1.2. Energy.** Despite the stable operation of the Nd:YAG laser, characterised by small fluctuations of approximately 5% (C.I. 95%) around the mean incident energy value, the energy deposited in the flow in each spark event actually exhibits great variation. This is shown in figure 4 in terms of pdfs of absorbed energy,  $E_{\text{abs}}$ , for the three spray conditions and low and high incident energies. Fluctuations of up to 90% of the mean absorbed energy value for low incident energy are observed, while that value was 20% for high incident energy. Furthermore, the effect of the SMD on the absorbed energy seems to be more significant at low incident energy, in which the coarse spray ( $d_{32} = 27 \mu\text{m}$ ) led to typically lower absorbed energy. Two effects are in play and are expected to affect the energy absorption process. First,

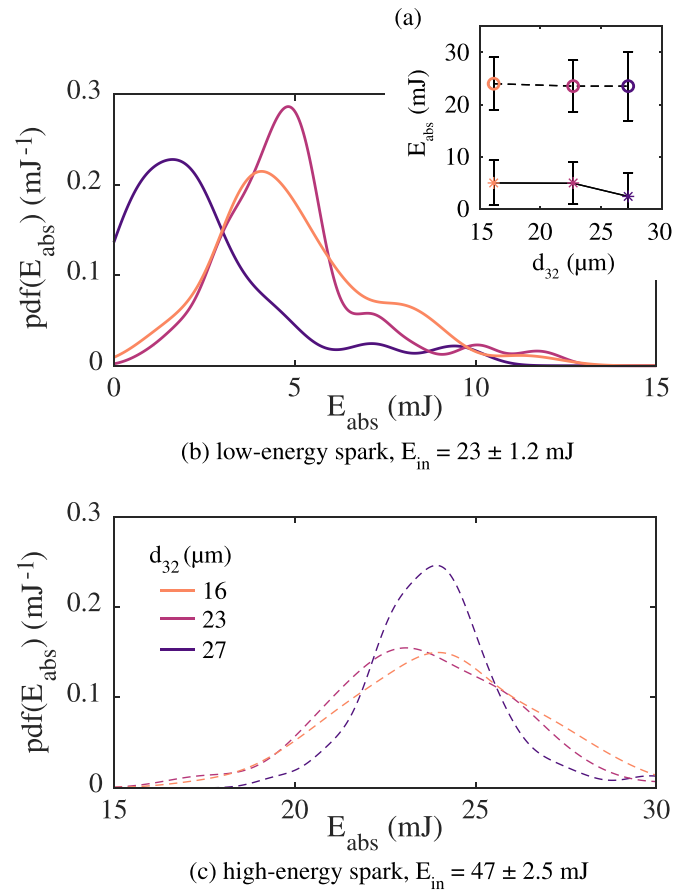


**Figure 4.** Pdfs of absorbed energy at the spark location in terms of the SMD for fine to coarse sprays ( $d_{32} = 16\text{--}27 \mu\text{m}$ ) and low and high incident laser energies ( $E_{\text{in}} =$  (b) 23 and (c) 47 mJ). The detail plot shows the mean absorbed value.

if the laser energy is lower than the minimum required for excitation and atomisation of the mixture—as different species have distinct excitation energies—the amount of ionised molecules will be dependent on the local mixture. These molecules ionised through a multi-photon process release the necessary seed electrons that absorb more photons, thus colliding with other molecules and ionizing them and, in turn, leading to further energy absorption, an electron avalanche, and breakdown of the mixture [8]. Therefore, different local compositions would lead to different plasma volumes and different amount of energy absorbed between distinct spark events. Second, the presence of droplets has also optical effects on the beam path, increasing locally the fluence of the beam and thus facilitating breakdown, as mentioned previously [13, 14]. In a non-reacting gaseous atmosphere, for instance, breakdown is always achieved at absorbed energies of approximately 10 mJ in the current setup. Moreover, the higher the incident energies, the larger the focusing region of the laser path with the required fluence for breakdown and the larger the ‘sampling’ volume of the two-phase mixture (figure 3). This in turn is expected to lead to more consistent excitation of the species, lower fluctuations of absorbed energy and of plasma volume and composition, thus enhancing ignition (figure 5).

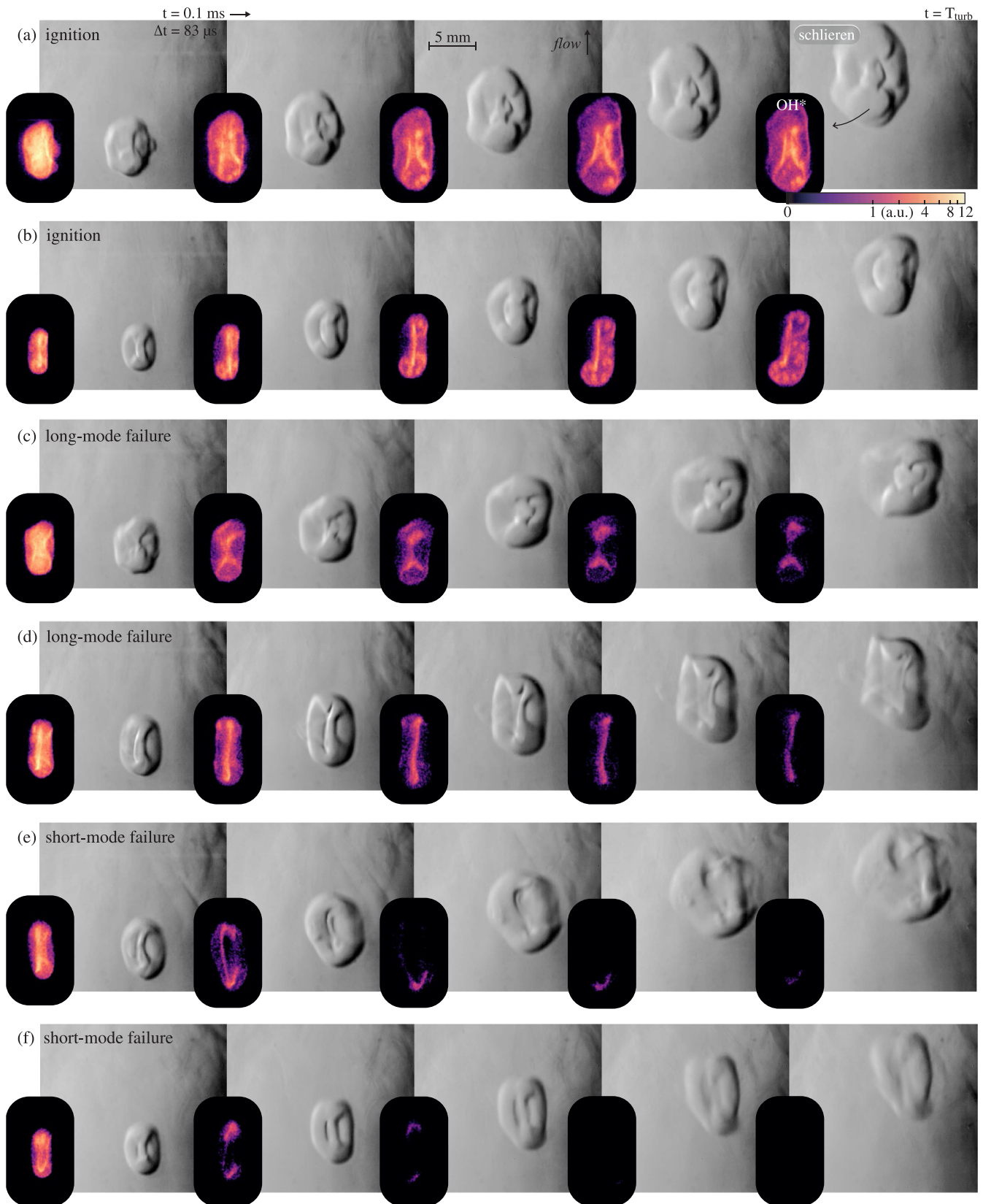


**Figure 5.** Schlieren (gray scale) and OH\* (log color scale) image sequences of the flame kernel during (a) and (b) ignition, (c) and (d) long-mode failure, and (e) and (f) short-mode failure events— $\phi = 0.8$ ,  $d_{32} = 16 \mu\text{m}$ ,  $E_{\text{in}} = 23 \text{ mJ}$ .

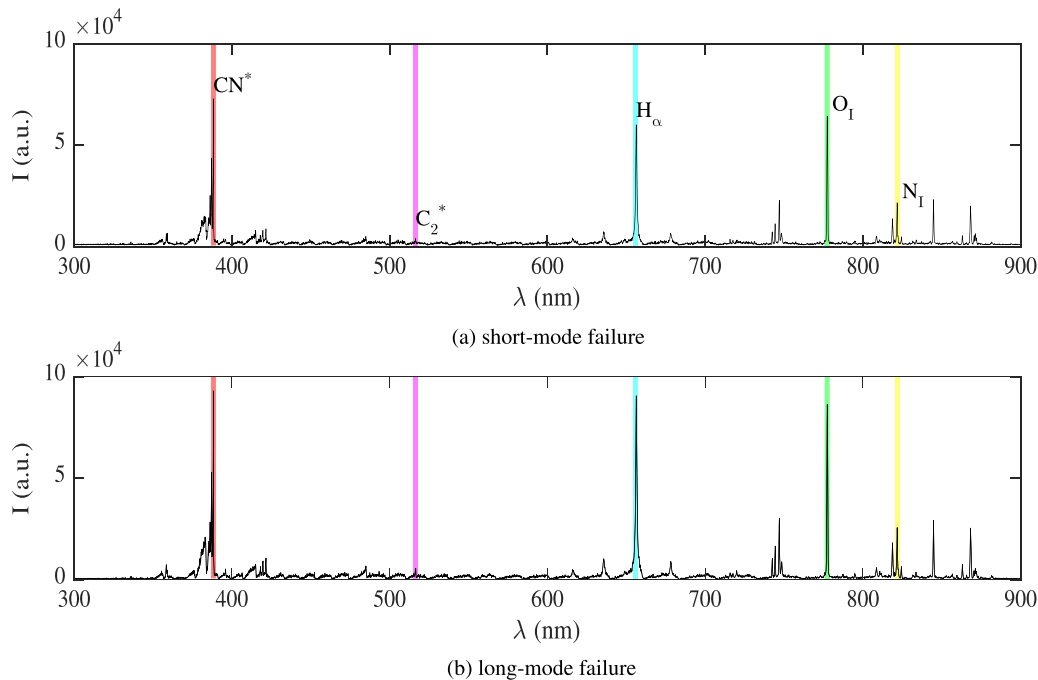


**Figure 6.** Cumulative plasma spectra for (a) short-mode ignition failure events (failed flame kernel establishment) and (b) long-mode ignition failure events (successful flame kernel establishment) –  $\phi = 0.8$ ,  $d_{32} = 16 \mu\text{m}$ ,  $E_{\text{in}} = 23 \text{ mJ}$ .

### 3.2. Towards understanding of plasma-flame transition

As an attempt to identify the differences between the success or failure to establish a flame kernel from the spark-generated plasma—that is, between short-mode failure events and events marked either by long-mode failure or ignition—we first illustrate the problem with characteristic image sequences of the flame kernel in figure 5 undergoing (a) ignition, (b) long-mode failure and (c) short-mode failure as visualised by schlieren and  $\text{OH}^*$  imaging. Then, the spectroscopic information of the plasma is introduced in figure 6 for the same flow condition and incident laser energy, conditioned to (a) short- and (b) long-mode failure.

Typical of laser-ignition experiments in a jet, the millimetre-sized flame kernel formed by the spark is imaged at  $100 \mu\text{s}$  after the laser pulse (i.e. at about the end of the plasma-related processes, early Phase 1b) and during a time interval of approximately that of the flow's integral time scale (1.2 ms). During this short window, the kernel may either grow or quench, being advected in the direction of the mean flow (upwards). If only schlieren imaging is used, one cannot assess the reactivity of the mixture within the kernel region, that is, distinguish a hot gas blob from a vigorously burning flame. As seen in the  $\text{OH}^*$  details of the image sequences, ignition ((a) and (b)) is marked by a strong  $\text{OH}^*$  signal, with peak regions that represent combustion in the vicinity of large droplets. In contrast, a slowly or abruptly fainting  $\text{OH}^*$  signal is observed in the ((c) and (d)) long and ((e) and (f)) short modes of ignition failure. The connection between the plasma characteristics, the initial flame kernel formed and the outcome of an ignition event are unclear.

In figure 6, each sub-figure shows the cumulative spectrum concerning many events of a given category out of a

total of 120 spark events for this condition (16  $\mu\text{m}$  SMD, 23 mJ incident energy). Several emission lines can be identified in both cases. The  $\text{H}_\alpha$  Balmer line and  $\text{O}_I$  atomic line are clearly visible at 656.3 nm and 777.3 nm, respectively, the former originating from dissociated hydrogen from hydrocarbon molecules and the latter from dissociated oxygen molecules in air. Similarly,  $\text{N}_I$  atomic lines are also present, e.g. at 821.6 nm. A strong  $\text{CN}^* B^2\Sigma^+ - X^2\Sigma^+$  molecular band is found (peak at 388.3 nm), originating from the recombination of carbon and nitrogen dissociated from fuel and air [29]. The  $\text{C}_2^* d^3\Pi_g - a^3\Pi_u$  band, which peaks at 516.5 nm, is also characteristic of hydrocarbon fuels and visible, although very weak in the cumulative spectrum in comparison to other lines. Other than the fact that events where a flame kernel was established (figure 6(b)) exhibit somewhat higher  $\text{CN}^*$ ,  $\text{C}_2^*$ ,  $\text{H}_\alpha$ , and  $\text{O}_I$  emission levels, not much can be said about the differences between short-mode and long-mode failure events.

The individual spectra used to obtain the cumulative spectrum shown in figure 6 exhibited great event-to-event variation. This was expected, as both mixture and energy deposited in each spark event were also expected to vary from event to event [12]. Although the ignition process is understood to be affected by such fluctuations through the resulting composition and temperature of the kernel [1], it is a challenging task, if not impossible, to experimentally evaluate the impact of chemical and thermal effects independently of each other (e.g. by holding the plasma temperature constant while varying its composition). As the plasma temperature is not directly measured in the present experiments, a statistical approach is needed to assess the impact of plasma composition on the process. Next, we discuss these fluctuations in terms of the emission lines previously highlighted. Each emission value for a different species is evaluated as

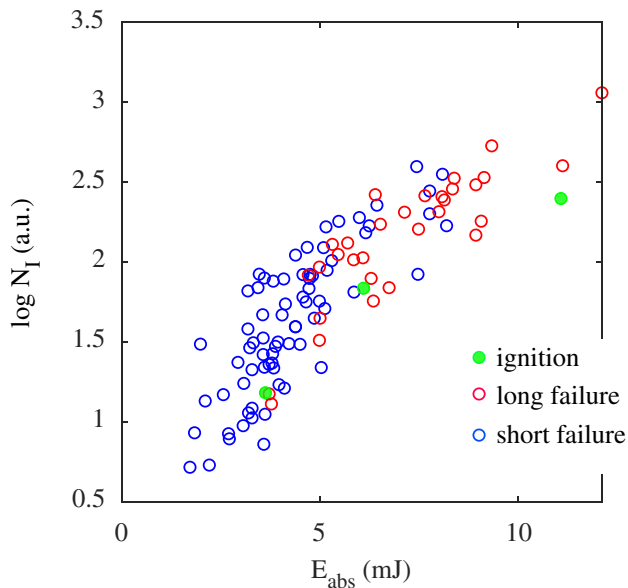


**Figure 7.**  $N_1$  emissions versus energy absorbed in each event. Jet A,  $\phi = 0.8$ ,  $d_{32} = 16 \mu\text{m}$ ,  $E_{in} = 23 \text{ mJ}$ .

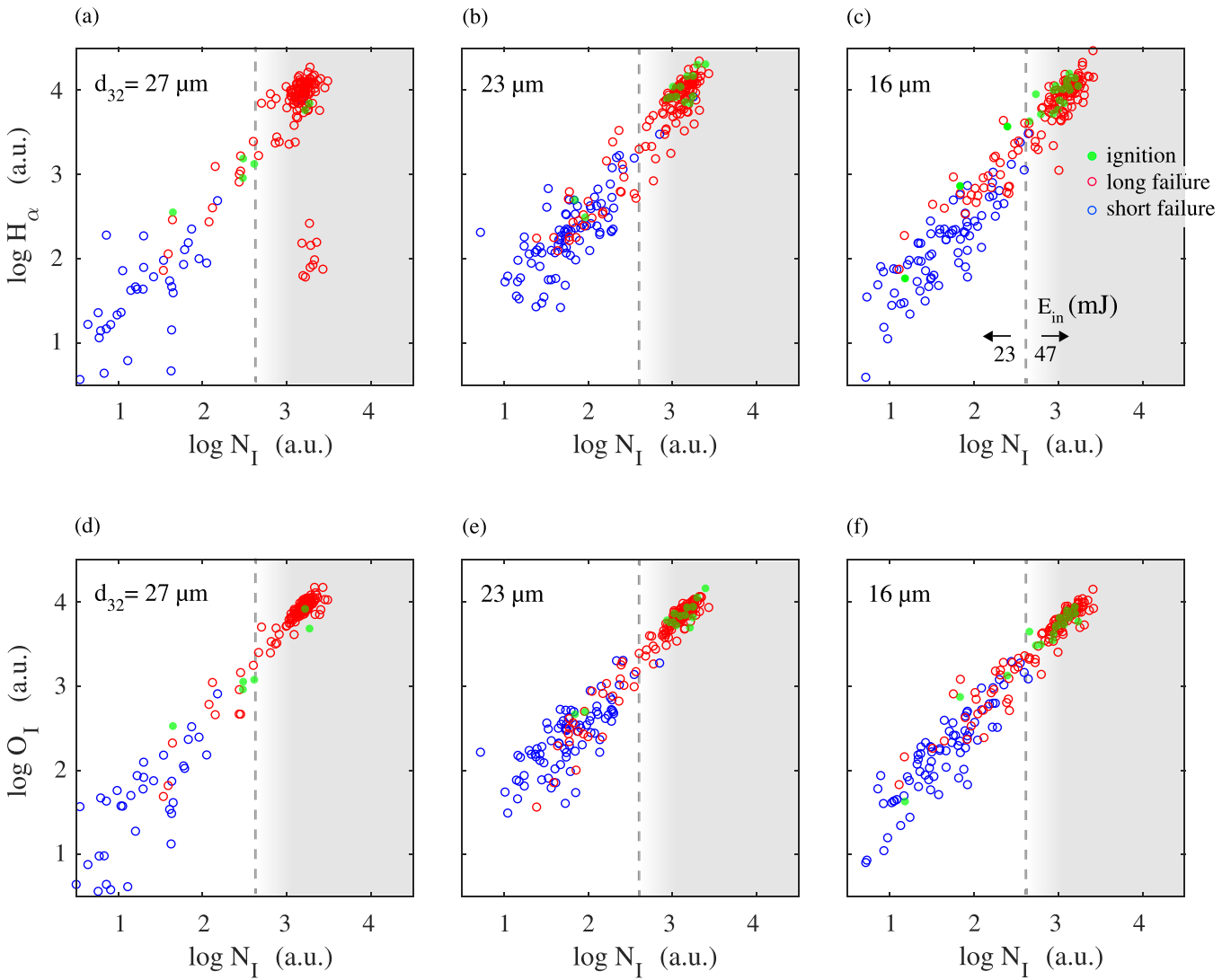
the intensity measured at the CCD sensor integrated over the full-width half-max around the peak. As our interest lies in assessing the impact of the *concentration* of a given species in the radical pool on the establishment of the flame kernel, we look at emissions in terms of  $N_1$  emissions as a reference.  $N_1$  emissions span linearly with the laser energy absorbed, as illustrated in figure 7 (16  $\mu\text{m}$  SMD, 23 mJ incident energy)—high emission intensities suggest both a high plasma temperature as well as a large plasma size. Thus, individual species' emissions are interpreted relative to  $N_1$  emissions, representative of the amount of air present and excited by the laser spark (hence providing a measure of the relative concentration of a given species in the plasma) and, to some extent, representative of the approximate plasma temperature. Additionally, as the absolute intensity of the species' emissions increases exponentially with the absorbed energy, understanding emission intensities in light of  $N_1$  emissions as a reference can be convenient to account for energy fluctuations inherent of the process in experiments where the absorbed energy is not measured.

Figure 8 depicts how  $H_\alpha$  and  $O_1$  may impact on the ignition process. It shows the emissions for each spark event out of 120 attempts, with  $H_\alpha$  in the top row and  $O_1$  in the bottom row, for coarse to fine sprays (left to right). As results for low and high incident energies are shown, a dashed line and different backgrounds roughly separate the two data sets—despite the high confidence interval, some outliers are present. Events fall in three categories: (blue) short-mode failure, in which a kernel is formed but not established, (red) long-mode failure, in which a kernel is formed and established, and (green) ignition, in which a self-sustained flame is observed at the end of the process. First, one should note that in the coarse spray ((a) and (d)), a smaller number of events at low incident energy is observed since breakdown of the mixture is more challenging

at those conditions [12]. Greater variation of both (a)  $H_\alpha$  and (d)  $O_1$  emissions can be noted at those conditions, especially at very low  $N_1$  values, representative of low absorbed energy and small plasma size. This effect is expected to be a combination of higher mixture fluctuations at smaller plasma sizes, as well as to the partial excitation of the mixture present due to the extremely low energies deposited in the flow. As the absorbed energy increases, lower variations are expected, as seen in the experiments—an effect that seems to be greater than that occurring due to the change in SMD from 23  $\mu\text{m}$  to 16  $\mu\text{m}$ .

To establish a kernel—chain branching reactions leading to net positive radical production—a high ratio of hydrogen to nitrogen emissions seems to be necessary, that is, a high concentration of hydrogen excited atoms in the plasma. Most long-mode failure events (red markers, figure 8) exhibited high  $H_\alpha$  emission levels. In particular, events in which successful ignition was observed (green markers) were characterised by high  $H_\alpha$  emissions. A group of outliers is shown in figure 8(a) at high incident energy and low  $H_\alpha$  emissions; these could be related to spark events in which breakdown occurs in the absence of droplets at the spark, with only fuel vapour present. For that, high absorbed energy is needed, near the threshold value of 10 mJ previously found for breakdown of a pure gaseous mixture. Few events of this type can be seen at the right tail of the pdf in figure 4(b)(23  $\mu\text{m}$ ). Further, in contrast to the  $H_\alpha$  emission data, a wider range of  $O_1$  emissions was verified in both long-mode failure and ignition events. While high variations of  $O_1$  emissions are observed for low  $N_1$  values or absorbed energies, small variations are observed for high  $N_1$  values, especially in comparison to emissions levels of fuel-derived species (figures 8 and 10).

The present experimental evidence on the role of hydrogen radicals in the ignition process, deriving from the local presence of droplets at the spark location, seems to corroborate numerical findings obtained in direct numerical simulations (DNS). DNS findings [17, 30] indicate that the generation of a mixture with optimum equivalence ratio at the spark location is key to the establishment of a flame kernel. For instance, if evaporation of the droplets surrounding the spark lead to a near-stoichiometry or rich gas phase, heat release in that area is observed to be maximised, allowing for a thermal runaway process to occur and, at the same time, diffusion of energy towards the surroundings of the spark, which, in turn, allows for further fuel evaporation leading to flame propagation. Even in purely gaseous mixtures, the presence of fuel inhomogeneities is known to enhance ignition of overall lean mixtures, while ignition of locally lean mixtures can only be achieved with significantly higher energies [31]. Furthermore, as discussed by Gebel *et al* [15] in the context of LIBS experiments, the availability of hydrogen in the radical pool is key to ignition, as those recombine with oxygen radicals to form  $\text{OH}^*$  [15]. With that in mind, we report the  $\text{OH}^*$  intensity of the flame kernel early in Phase 1b (figure 1), which results from the plasma processes and early fuel pyrolysis in the kernel. The  $\text{OH}^*$  signal normalised by flame unit area imaged from 100 to 180  $\mu\text{s}$  after the spark is given in figure 9 together with the



**Figure 8.**  $H_{\alpha}$  (656.3 nm) and  $O_I$  (777.3 nm) emissions in terms of  $N_I$  (821.6 nm) emissions conditioned to short-mode and long-mode failure and ignition—Jet A,  $\phi = 0.8$ ,  $d_{32} = 16\text{--}27\ \mu\text{m}$ .

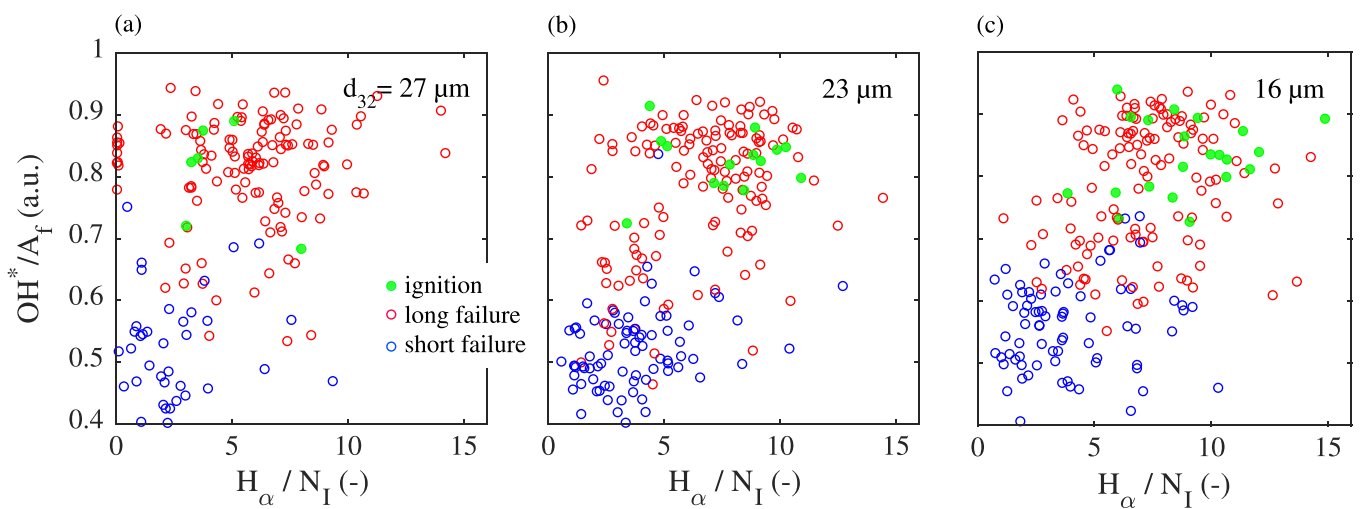


**Figure 9.**  $OH^*$  signal normalised by flame area imaged at  $100\ \mu\text{s}$  and  $H_{\alpha}/N_I$  emissions in the plasma—Jet A,  $\phi = 0.8$ ,  $d_{32} = 16\text{--}27\ \mu\text{m}$ .

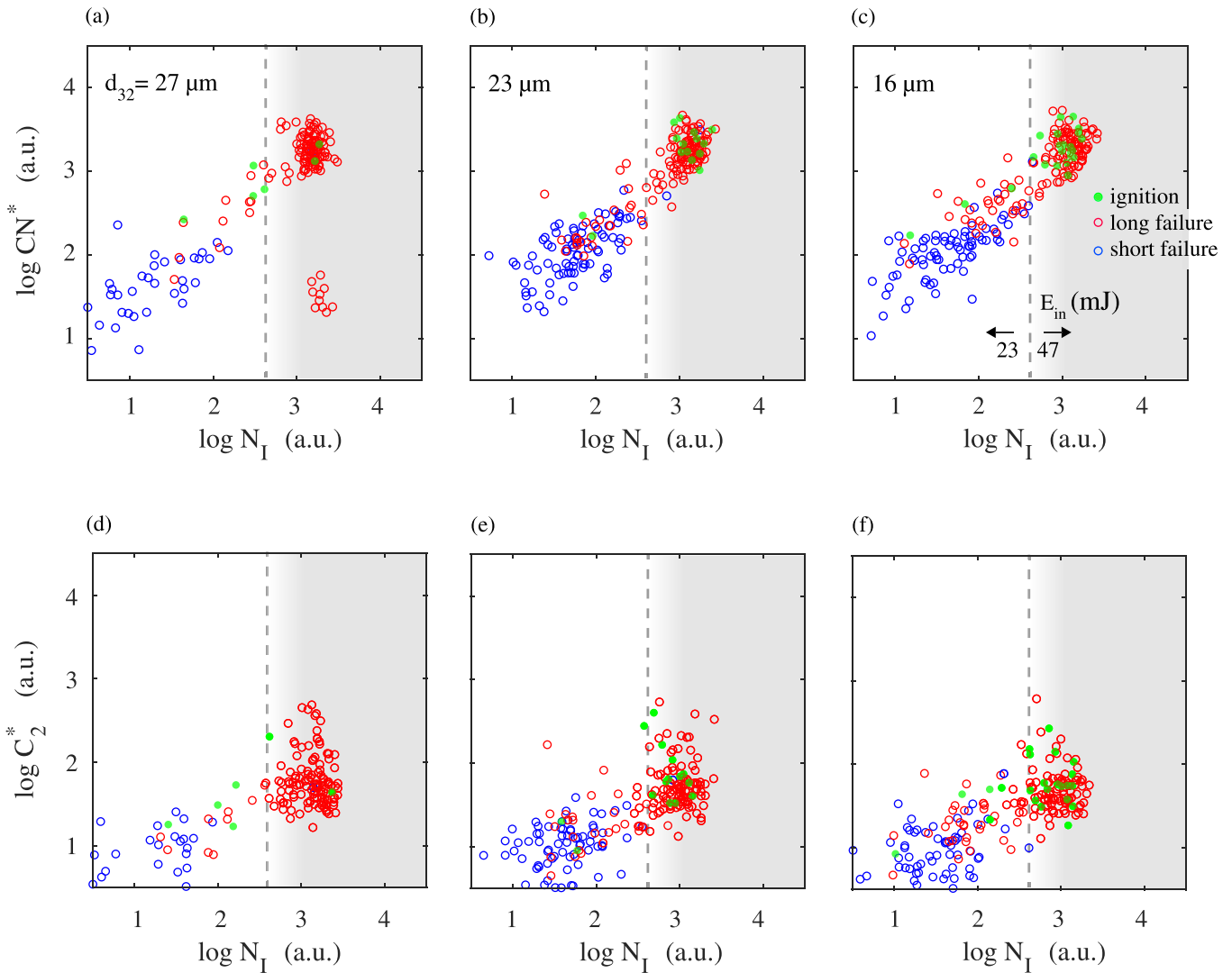


**Figure 10.**  $C_2$  (516.5 nm) and  $CN^*$  (388.3 nm) emissions in terms of  $N_I$  (821.6 nm) emissions conditioned to short-mode and long-mode failure and ignition—Jet A,  $\phi = 0.8$ ,  $d_{32} = 16\text{--}27\ \mu\text{m}$ .

ratio of  $H_\alpha$  to  $N_I$  emissions. Despite the great scatter in the results, a positive correlation between the two can be observed. Decreasing the SMD from (a) to (c) led to a shift from short-mode (blue) to long-mode failure (red), that is, flame kernels survived for longer times in the flow

Similarly to  $H_\alpha$ , high levels of  $CN^*$  and  $C_2^*$  emissions were also found in long-failure events and ignition events (figure 10).  $CN^*$  emissions are stronger by at least one order of magnitude than  $C_2^*$ , similar to what has been observed in previous experiments [11]. Additionally,  $C_2^*$  emissions exhibited the greatest variation at high energy conditions in comparison to all the emissions of all species investigated in this study. Typically,  $C_2^*$  emission lines are characteristic of overall rich mixture conditions (mean equivalence ratio between 6 and 10) [5, 29] and high liquid loading [7]. Both  $CN^*$  and  $C_2$  seem to originate from the recombination of fuel-derived plasma radicals [15], hence also depending on the local instantaneous equivalence ratio at the spark location. The establishment of the kernel is believed to also depend on high concentration of  $C_2$  in the plasma, which reacts with ground-state OH to

form  $CH^* + CO$ —an important formation paths of hydrocarbon flames [15].

#### 4. Conclusion

An experimental approach was presented to assess the impact of the plasma composition on the transition from plasma to flame kernel to self-sustained flame during the ignition of sprays. LIBS was used to evaluate  $H_\alpha$ ,  $CN^*$ ,  $C_2^*$ ,  $O_I$  and  $N_I$  emissions in the flame kernel within the first 50  $\mu\text{s}$  from the spark, followed by  $OH^*$  imaging. The  $OH^*$  signal was normalised by the flame area imaged, used to evaluate the average time to the net increase of chain-branching reactions, here defined as critical time scale. Ignition terminology and definitions were revised based on that time scale, so that the distinction between kernel generation and flame growth can be experimentally assessed. This approach allowed for the plasma emissions to be quantified and conditioned based on the establishment of a flame kernel, a process dominated by

plasma decomposition, recombination which then lead to combustion reactions, that is, independently of the subsequent flame growth phase, which is mostly controlled by flame-propagation phenomena such as fuel availability and flame strain.

The stochasticity of ignition was then understood in light of the kernel generation process and its combined fluctuations related to laser energy, breakdown and radical generation processes, as well as local mixture fluctuations inherent of two-phase flows. A simple stochastic model was proposed to illustrate the degree of mixture fluctuations expected at the spark location. It showed that, in sprays with a SMD from 16 to 27  $\mu\text{m}$  and plasma sizes between 0.4 and 1 mm, fluctuations of equivalence ratio can be expected up to over twice the overall (mean) equivalence ratio of the flow. That, together with laser energy fluctuations, seem to have impacted on the hydrogen emissions which derive from fuel decomposition in the breakdown plasma. Preliminary results indicate that in order to successfully establish a kernel, that is, obtain a net-positive gain of radicals through chain-branching reactions, a high concentration of H in the breakdown plasma is needed. Self-sustained flame propagation is observed for the highest levels of  $\text{H}_\alpha$  and  $\text{CN}^*$  emissions. Confirming previous evidence, experiments indicate that the high availability of hydrogen seems to allow for recombination with oxygen to form  $\text{OH}^*$  in large quantities, then leading to the main formation paths of hydrocarbon flames.

The present framework allows for further development of LIBS towards ignition and engine-health devices that can be employed in aerospace applications. For that, future work will include a more detailed account of the plasma-flame kinetics in sprays by focusing, for example, on the temporal evolution of key species' emissions such as  $\text{H}_\alpha$ ,  $\text{OH}^*$  and  $\text{CH}^*$  throughout the process—from the breakdown of the mixture and recombination processes, through on-set of chain-branching reactions of the kernel. Additionally, the development of LIBS as an accurate point-wise technique for air-fuel ratio measurements in sprays will also be further explored by combining the present stochastic model with careful calibration procedures to obtain local-instantaneous measurements and, with that, reduce the large uncertainties currently associated with this technique.

### Data availability statement

The data that support the findings of this study are available upon reasonable request from the authors.

### Acknowledgments

PMO kindly acknowledges the financial support of the Brazilian Space Agency and Brazil's National Council for Scientific and Technological Development (Project #203086/2015-5). EM, MK and PMO acknowledge the European Commission Clean Sky 2 project PROTEUS (785349).

### ORCID iDs

Pedro M de Oliveira  <https://orcid.org/0000-0002-5527-8128>

Michael Philip Sitte  <https://orcid.org/0000-0002-7502-9858>

Patton M Allison  <https://orcid.org/0000-0001-7819-2303>

Epaminondas Mastorakos  <https://orcid.org/0000-0001-8245-5188>

### References

- [1] Mastorakos E 2009 Ignition of turbulent non-premixed flames *Prog. Energy Combust. Sci.* **35** 57–97
- [2] Phuoc T X and White F P 2002 Laser-induced spark for measurements of the fuel-to-air ratio of a combustible mixture *Fuel* **81** 1761–5
- [3] Michalakou A, Stavropoulos P and Couris S 2008 Laser-induced breakdown spectroscopy in reactive flows of hydrocarbon-air mixtures *Appl. Phys. Lett.* **92** 081501
- [4] Tripathi M M, Srinivasan K K, Krishnan S R, Yueh F-Y and Singh J P 2013 A comparison of multivariate LIBS and chemiluminescence-based local equivalence ratio measurements in premixed atmospheric methane-air flames *Fuel* **106** 318–26
- [5] Kotzagianni M, Yuan R, Mastorakos E and Couris S 2016 Laser-induced breakdown spectroscopy measurements of mean mixture fraction in turbulent methane flames with a novel calibration scheme *Combust. Flame* **167** 72–85
- [6] Yuan R, Kotzagianni M and Couris S 2014 Laser-induced breakdown spectroscopy measurements in spray flames *17th Int. Symp. on Applications of Laser Techniques to Fluid Mechanics (Lisbon)*
- [7] Lee S H, Do H and Yoh J J 2016 Simultaneous optical ignition and spectroscopy of a two-phase spray flame *Combust. Flame* **165** 334–45
- [8] Phuoc T X 2006 Laser-induced spark ignition fundamental and applications *Opt. Lasers Eng.* **44** 351–97
- [9] Moesl K G, Vollmer K G, Sattelmayer T, Eckstein J and Kopecek H 2009 Experimental study on laser-induced ignition of swirl-stabilized kerosene flames *J. Eng. Gas Turbines Power* **131** 021501
- [10] Ferioli F, Puzinauskas P V and Buckley S G 2003 Laser-induced breakdown spectroscopy for on-line engine equivalence ratio measurements *Appl. Spectrosc.* **57** 1183–9
- [11] Beduneau J L, Kawahara N, Nakayama T, Tomita E and Ikeda Y 2009 Laser-induced radical generation and evolution to a self-sustaining flame *Combust. Flame* **156** 642–56
- [12] de Oliveira P M, Sitte M P and Mastorakos E 2019 Validation of a low-order model for ignition of sprays *57th AIAA Aerospace Sciences Meeting* pp 1–6
- [13] Müsing A, Riedel U, Warnatz J, Herden W and Ridderbusch H 2007 Laser-induced breakdown in air and behind droplets: a detailed Monte-Carlo simulation *Proc. Combust. Inst.* **31** 3007–14
- [14] El-Rabii H, Gaborel G, Lapios J-P, Thévenin D, Rolon J C and Martin J-P 2005 Laser spark ignition of two-phase monodisperse mixtures *Opt. Commun.* **256** 495–506
- [15] Gebel G C, Mosbach T, Meier W and Aigner M 2015 Optical and spectroscopic diagnostics of laser-induced air breakdown and kerosene spray ignition *Combust. Flame* **162** 1599–613
- [16] Mastorakos E 2017 Forced ignition of turbulent spray flames *Proc. Combust. Inst.* **36** 2367–83

- [17] Wandel A P, Chakraborty N and Mastorakos E 2009 Direct numerical simulations of turbulent flame expansion in fine sprays *Proc. Combust. Inst.* **32** 2283–90
- [18] Cardin Celine, Renou B, Cabot G and Boukhalfa A M 2013 Experimental analysis of laser-induced spark ignition of lean turbulent premixed flames: new insight into ignition transition *Combust. Flame* **160** 1414–27
- [19] Gebel G C, Mosbach T, Meier W and Aigner M 2015 Laser-induced blast waves in air and their effect on monodisperse droplet chains of ethanol and kerosene *Shock Waves* **25** 415–29
- [20] Lefebvre A H 1988 *Atomization and Sprays* 1st edn (Boca Raton, FL: CRC Press)
- [21] Pope S B 2000 *Turbulent Flows* (Cambridge: Cambridge University Press)
- [22] de Oliveira P M and Mastorakos E 2019 Mechanisms of flame propagation in jet fuel sprays as revealed by OH/fuel planar laser-induced fluorescence and OH\* chemiluminescence *Combust. Flame* **206** 308–21
- [23] Edwards J T 2017 Reference jet fuels for combustion testing *55th AIAA Aerospace Sciences Meeting* (Reston: American Institute of Aeronautics and Astronautics)
- [24] Coleman H W and Steele W G 2009 *Experimentation, Validation and Uncertainty Analysis for Engineers* 3rd edn (Hoboken: Wiley)
- [25] Moffat R J 1988 Describing the uncertainties in experimental results *Exp. Therm. Fluid Sci.* **1** 3–17
- [26] de Oliveira P M, Sitte M P and Mastorakos E 2022 Polydispersity effects in low-order ignition modeling of jet fuel sprays *Combust. Sci. Technol.* **194** 258–271
- [27] de Oliveira P M, Sitte M P, Zedda M, Giusti A and Mastorakos E 2021 Low-order modeling of high-altitude relight of jet engine combustors *Int. J. Spray Combust. Dyn.* **13** 20–34
- [28] Rizk N K and Lefebvre A H 1985 Drop-size distribution characteristics of spill-return atomizers *J. Propulsion Power* **1** 16–22
- [29] Kotzagianni M, Yuan R, Mastorakos E and Couris S 2014 Laser-induced breakdown spectroscopy measurements in turbulent methane flames *52nd Aerospace Sciences Meeting* (Reston, VA: American Institute of Aeronautics and Astronautics)
- [30] Neophytou A, Mastorakos E and Cant R S 2010 DNS of spark ignition and edge flame propagation in turbulent droplet-laden mixing layers *Combust. Flame* **157** 1071–86
- [31] Chakraborty N and Mastorakos E 2008 Direct numerical simulations of localised forced ignition in turbulent mixing layers: the effects of mixture fraction and its gradient *Flow Turbul. Combust.* **80** 155–86